ADVANCED MATERIALS
www.advmat.de

# High Performance P-Channel Transistor Based on Amorphous Tellurium Trioxide

*Seungho Bang, Chaewon Lee, Deogkyu Choi, Dae Young Park, Dong Hyeon Kim, Dohyeon Lee, Dong-Joon Yi, Jungeun Song, Seok Joon Yun, Dong-Wook Kim,* and Mun Seok Jeong**

**The development of high-performance p-channel transistors remains a critical challenge in complementary logic circuits, despite significant advances in n-channel transistor technologies. While amorphous oxide semiconductors have revolutionized n-type transistors, achieving comparable performance for p-type counterparts has proven elusive. Here, this study demonstrates a breakthrough in p-channel technology by transforming crystalline 2D tellurium (2D-Te) into amorphous tellurium trioxide (a-$TeO_3$) through UV ozone treatment. This structural transformation, directly observed via high-resolution transmission electron microscopy, induces dramatic changes in electronic properties, including significant bandgap widening and enhanced work function. The resulting a-$TeO_3$-based p-channel transistors demonstrate remarkable improvements over crystalline 2D-Te transistors, featuring reduced hysteresis, superior on/off characteristics, and distinctive mobility behavior at different temperatures and gate fields. Most notably, these transistors achieve exceptionally low barrier height (10 meV) and sheet resistance values, while combining high hole mobility with excellent switching properties. The work not only introduces a novel high-performance p-channel semiconductor but also opens new avenues for phase engineering in advanced semiconductor development.**

## 1. Introduction

As conventional silicon-based technologies approach their fundamental physical limitations in device scaling, the search for alternative semiconductor materials has intensified. 2D semiconductors have emerged as promising candidates for next-generation electronics, offering exceptional carrier transport properties and superior electrostatic control at atomic thicknesses.[1] These unique properties make 2D materials particularly attractive for low-power complementary metal-oxide-semiconductor (CMOS) applications, where minimal leakage current and excellent gate control are essential for reducing power consumption. Despite the promising potential of 2D materials for low-power CMOS technology, n-type 2D semiconductors have been extensively studied for their strong electron doping due to interfacial charge impurities and intrinsic structural defects, but the development of high-performance p-type transistors comparable to n-type semiconductors remains a significant challenge.[2,3]

Among various 2D p-type semiconductors, black phosphorus initially garnered significant attention due to its unique electronic properties, including thickness-dependent direct bandgap (0.3–2.0 eV) and remarkable hole mobility exceeding 1000 $cm^2\ V^{-1}\ s^{-1}$.[4] However, the extreme sensitivity of black phosphorus to ambient conditions results in rapid degradation, severely hindering its practical applications, especially in the development of stable p-channel transistors. Transition metal dichalcogenides (TMDs), particularly tungsten diselenide ($WSe_2$), have emerged as alternative p-type candidates, demonstrating improved stability and reasonable hole mobility.

S. Bang, C. Lee, D. Choi, D. Y. Park, D. H. Kim, D. Lee, D.-J. Yi, M. S. Jeong
Department of Physics
Hanyang University (HYU)
Seoul 04763, Republic of Korea
E-mail: mjeong@hanyang.ac.kr

The ORCID identification number(s) for the author(s) of this article can be found under https://doi.org/10.1002/adma.202504948



**DOI: 10.1002/adma.202504948**

D.-J. Yi
Department of Electronics Engineering
Hanyang University (HYU)
Seoul 04763, Republic of Korea

J. Song, D.-W. Kim
Department of Physics
Ewha Womans University
Seoul 03760, Republic of Korea
E-mail: dwkim@ewha.ac.kr

S. J. Yun
Department of Semiconductor Physics and Engineering
University of Ulsan
Ulsan 44610, Republic of Korea

Advances in $WSe_2$-based transistors have achieved hole mobilities of ≈250 $cm^2 V^{-1} s^{-1}$ with enhanced on/off ratios exceeding $10^6$, representing significant progress in p-type 2D semiconductor development.[5] Despite these improvements, challenges remain in achieving consistent performance and reliable doping control in TMD-based p-type transistors.[6–9] This challenge of achieving both high mobility and satisfactory on/off ratios is not unique to 2D semiconductors but extends to the broader field of p-type semiconductor development. In amorphous semiconductor systems, the development of high-performance p-type materials has been notably difficult. While n-type amorphous oxide semiconductors have achieved electron mobilities exceeding 10 $cm^2 V^{-1} s^{-1}$ with excellent switching characteristics, p-type amorphous oxide semiconductors typically exhibit hole mobilities below 1 $cm^2 V^{-1} s^{-1}$ with limited on/off ratios.[10] This limitation primarily stems from the inherent nature of hole transport in amorphous materials, where the strong localization of oxygen 2p orbitals at the valence band maximum leads to heavy hole effective masses and significant carrier scattering.[11] However, despite these encouraging advancements, the current mobility and switching characteristics have not yet met the performance levels necessary for practical CMOS applications and commercial p-channel transistor implementation, highlighting the need for further fundamental research and material enhancements.[12] In particular, 2D tellurium (2D-Te) has recently attracted attention as a promising p-type semiconductor, offering both enhanced environmental stability and high hole mobility (≈1000 $cm^2 V^{-1} s^{-1}$). However, its inherently narrow bandgap (≈0.3 eV) leads to semimetallic behavior with poor on/off ratios, severely limiting its application in practical transistors.[13] Various strategies to modulate its electronic structure, including thickness reduction and surface modification, have been explored but typically result in significantly degraded carrier transport properties.

One promising approach to overcome these obstacles is ultraviolet ozone (UV-$O_3$) processing, which has shown considerable success in fine-tuning the oxidation states of 2D materials for field-effect transistor (FET) applications. For example, Zheng et al. demonstrated that $MoTe_2$ can be oxidized layer-by-layer by $O_3$ exposure, forming oxide layers with atomic precision while preserving the crystal integrity of the underlying 2D material.[14] This technique offers several advantages, including effective surface passivation, oxidation-induced carrier doping, and the development of high-quality oxide interfaces.

In this study, we demonstrate a breakthrough in high-performance p-channel semiconductor development through amorphous tellurium trioxide (a-$TeO_3$) synthesized by precisely controlled UV-$O_3$ treatment of 2D-Te. This transformative approach fundamentally alters both structural and electronic properties of the material. High-resolution transmission electron microscopy (HRTEM) reveals a complete phase transformation from crystalline 2D-Te helical chains to a-$TeO_3$, while Raman spectroscopy confirms this change through the emergence of a new vibrational mode at 618 $cm^{-1}$ and the disappearance of pristine 2D-Te Raman peaks. This structural evolution leads to remarkable electronic modifications, with the bandgap expansion from 0.3 to 3.04 eV, effectively overcoming the inherent limitations of 2D-Te. Most significantly, we observe an extraordinarily low Schottky barrier height (SBH) of 10 meV at the metal-semiconductor interface, resulting in exceptional contact resistance ($R_c$: 626.81 Ω·μm). The a-$TeO_3$-based field-effect transistors demonstrate remarkable performance metrics, combining high hole mobility (238.6 $cm^2 V^{-1} s^{-1}$) with superior on/off ratio ($0.81 \times 10^5$), and a significantly reduced interface trap density ($2.69 \times 10^{14}$ $cm^{-2}$) compared to pristine 2D-Te ($6.50 \times 10^{14}$ $cm^{-2}$). Our comprehensive investigation establishes a-$TeO_3$ as a promising platform for next-generation p-channel transistors, offering a practical solution to the long-standing challenge of achieving both high hole mobility and excellent switching characteristics.

## 2. Results and Discussion

### 2.1. Controlled Phase Transformation: From Crystalline 2D-Te to Amorphous $TeO_3$

Crystalline 2D-Te exhibits a unique structural configuration characterized by 1D helical chains, where Te atoms are covalently bonded and aligned parallel to the z-axis, manifesting as a pseudo-low dimensional structure. **Figure 1a** shows 3D schematic illustrations of the amorphization of 2D-Te upon exposure to UV-$O_3$ treatment. The amorphization process, initiated from the top surface of 2D-Te through oxidation, progressively leads to the formation of completely phase-transformed a-$TeO_3$ as the UV-$O_3$ treatment time increases (Figure 1b). The detailed procedure for our crystalline 2D-Te synthesis method, as well as the thinning process used to remove polyvinylpyrrolidone, is provided in Figure S1 (Supporting Information). To identify the crystal structure more precisely, we performed cross-sectional HRTEM imaging and fast Fourier transform analysis, which confirmed the (001) plane in the 2D-Te layer near the substrate (Figure 1c,e). This plane aligns with the helical chain direction and is one of the fundamental crystallographic planes of $\beta$-Te, with a lattice spacing of ≈0.59 nm, which is close to the referenced values.[15,16] Careful TEM observations further revealed that the synthesized 2D-Te exhibits single crystalline properties; however, after UV-$O_3$ treatment, its crystallinity was lost and an amorphous a-$TeO_3$ phase formed on the surface (Figure 1d). This finding suggests that UV-$O_3$-induced oxidation disrupts the long-range order, eventually leading to complete amorphization. This oxidation process via UV-$O_3$ treatment is characteristically non-thermal, occurring rapidly on the timescale of femtoseconds ($10^{-15}$ s) to picoseconds ($10^{-12}$ s). In contrast, conventional thermal oxidation reactions require tens to hundreds of picoseconds for sufficient lattice heating and atomic rearrangement.[17,18] Therefore, UV-$O_3$ oxidation does not allow sufficient time for atoms to establish long-range order, resulting in the formation of an amorphous structure with limited long-range atomic arrangement. To confirm that the UV-$O_3$ treatment resulted in a fully amorphous structure of the thin 2D-Te layer, we performed additional HRTEM analysis. This analysis revealed a fully amorphized $TeO_3$, as shown in Figure S2 (Supporting Information). To probe the oxidation-induced phase transformation mechanism, X-ray photoelectron spectroscopy (XPS) analysis was employed to precisely quantify the chemical state and bonding of Te atoms. The XPS analysis reveals distinct chemical transformations through characteristic Te 3d core-level spectra. In the crystalline 2D-Te sample (Figure 1f), the spectrum exhibits complex peak deconvolution, featuring multiple oxidation states: $Te^0$ (metallic Te), $Te^{2+}$, and $Te^{4+}$, indicating partial natural

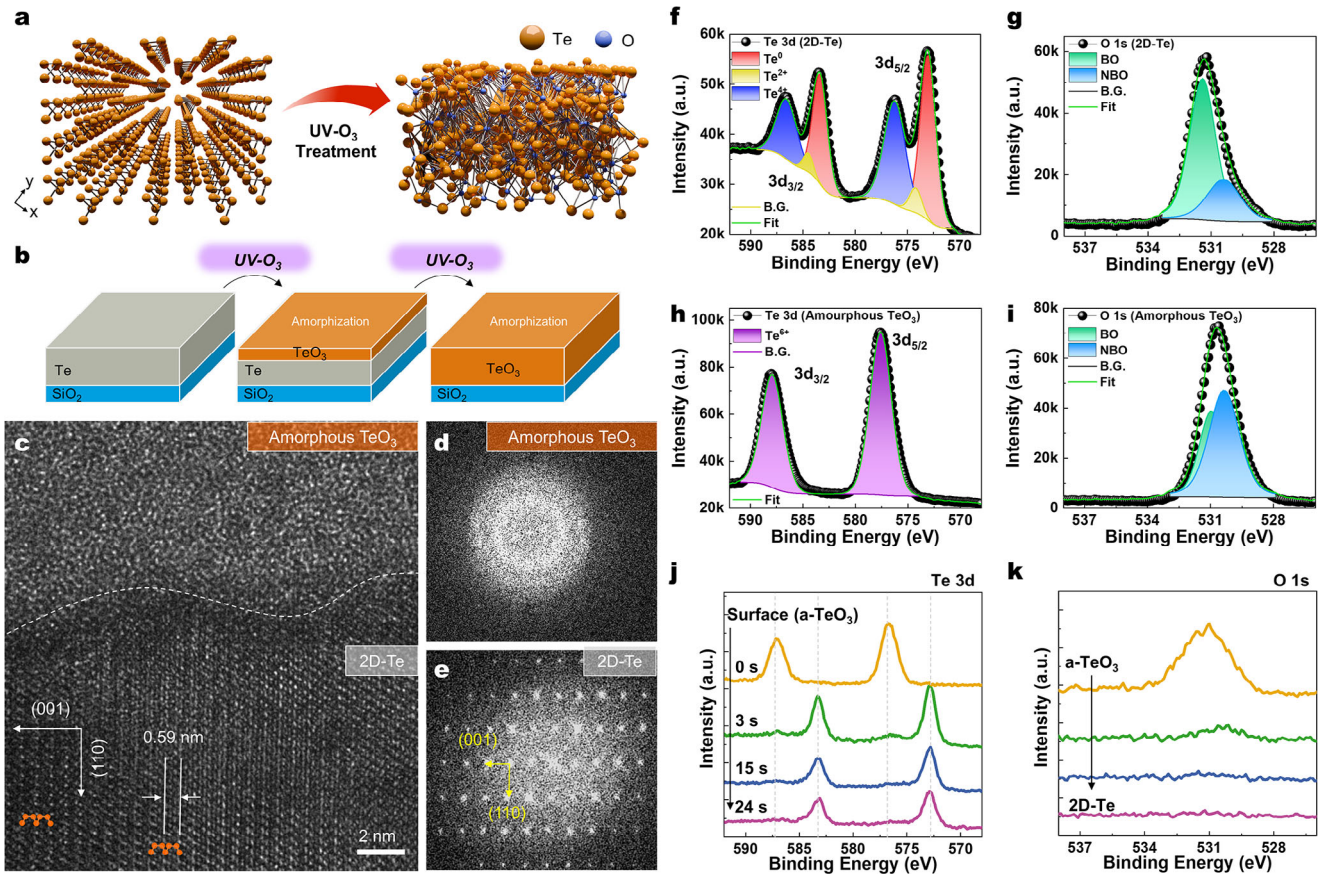


**Figure 1.** a) Schematic of the transformation of 2D tellurium (2D-Te) to amorphous tellurium trioxide (a-$TeO_3$) by UV-$O_3$ treatment. b) Cross-sectional diagram showing the phase transformation of 2D-Te to a-$TeO_3$ from the surface. c) High-resolution transmission electron microscope image clearly showing the interface between crystalline 2D-Te and amorphous $TeO_3$. The lattice spacing of 0.59 nm corresponding to the (110) plane of 2D-Te is highlighted. d) Fast Fourier Transform (FFT) pattern of a-$TeO_3$. e) FFT pattern of the crystalline 2D-Te region, indexed with (001) and (110) planes. f,g) XPS spectra of Te 3d and O 1s core-level peaks from pristine 2D-Te flakes. h,i) Corresponding XPS spectra (Te 3d and O 1s) obtained after 60 min UV-$O_3$ treatment, showing shifts indicative of chemical changes toward $TeO_3$ formation. XPS depth profiling spectra of Te 3d j) and O 1s k) core levels show the gradual transition from amorphous surface of a-$TeO_3$ to the underlying metallic 2D-Te as Ar-ion milling progresses (from 0 to 24 s; step of 3 s).

oxidation. The characteristic doublet structure of Te $3d_{3/2}$ and Te $3d_{5/2}$ exhibits a distinct energy separation of ≈10.4 eV.[19] Upon 60-min UV-$O_3$ treatment, the XPS analysis (Figure 1h) reveals remarkably resolved, monophasic binding energies at Te $3d_{3/2}$ (588 eV) and Te $3d_{5/2}$ (577.6 eV) characteristic of the $Te^{6+}$ oxidation state, demonstrating significantly enhanced peak intensity compared to the untreated sample.[20] This simplification of the spectral features and the complete conversion to $Te^{6+}$ provides compelling evidence for the successful formation of pure, a-$TeO_3$. The absence of lower energy states ($Te^0$, $Te^{2+}$, $Te^{4+}$) confirms the complete transformation of the material. The various oxidation states of Te, as reported in the literature, have been summarized in Table S1 (Supporting Information). This comprehensive analysis further confirms that the amorphous tellurium oxide formed under these conditions is a-$TeO_3$. To analyze the oxygen bonding states, we compared the O 1s peaks and observed that instead of the bridging oxygen (BO) mode in the covalent bonds of Te═O, the non-bridging oxygen (NBO) mode characteristic of a-$TeO_3$ dominates. NBO modes have lower binding energies than BO modes, indicating an increase in oxygen vacancies during the formation of the amorphous oxide semiconductor (Figure 1g,i).

A detailed discussion, which demonstrates that the observed BO and NBO peaks originate from the natural oxide layer of 2D-Te and the UV-$O_3$-treated a-$TeO_3$ layer, rather than the influence of the $SiO_2$ substrate, is provided in Figure S3 (Supporting Information). The presence of $Te^{6+}$ states was verified by survey results and additional XPS measurements, details of which are shown in Figure S4 (Supporting Information). To confirm that the UV-$O_3$ treatment not only affects the surface but also penetrates to a certain depth, we performed XPS depth profiling on the a-$TeO_3$/2D-Te sample prepared on a gold (Au) substrate using Ar-ion sputtering (4 keV, 6 µA, step time: 3 s), as shown in Figure 1j,k. The analysis revealed strong $Te^{6+}$ signals at the surface, while $Te^0$ signals became dominant in the bulk region as sputtering progressed. This indicates that the oxidation layer exists only up to a specific depth, with unoxidized $Te^0$ remaining beneath it. The O 1s signal disappeared completely after ≈9 s (three sputtering cycles), confirming the limited thickness of the oxidation layer and the presence of unoxidized $Te^0$ below it. Moreover, this UV-$O_3$ treatment process exhibits distinctly different phenomena compared to thermal oxidation (300°C, 1 h), as clearly demonstrated in Figure S5 (Supporting Information).

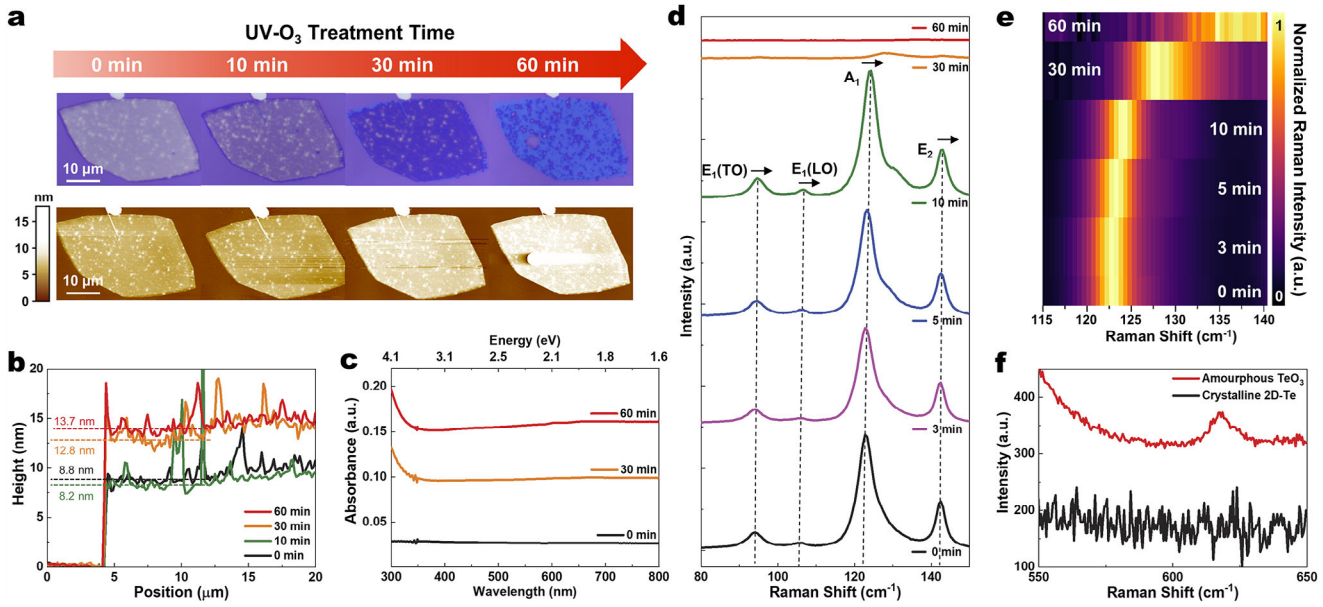


**Figure 2.** a) Time-dependent morphological evolution of 2D-Te under UV-$O_3$ treatment, visualized through OM (top row) and AFM (bottom row) images at 0, 10, 30, and 60 min intervals. OM images show gradual changes in optical contrast, while AFM topographical images reveal detailed surface morphology changes. Scale bars: 10 μm. b) Quantitative thickness analysis graph depicting four distinct phases of structural evolution during UV-$O_3$ treatment of 0, 10, 30, and 60 min intervals. The progression begins at 0 min with an initial thickness of ≈8 nm, representing pristine 2D-Te, followed by minimal change at 10 min. At 30 min, a significant increase to ≈12.8 nm indicates partial oxidation, reaching a final thickness of 13.7 nm at 60 min, confirming the complete transformation to a-$TeO_3$. c) Absorption spectra analysis revealing the optical bandgap expansion of a-$TeO_3$ formed after 30 min of UV-$O_3$ treatment, compared to pristine 2D-Te. The black line represents the initial state (0 min), showing the characteristic absorption of 2D-Te. The orange and red lines depict the spectra after UV-$O_3$ treatment, with the red line (60 min) indicating the formation of a-$TeO_3$ with an expanded bandgap. d) Time-dependent Raman spectroscopy data showing the structural transformation during the UV-$O_3$ treatment process. The graph displays the evolution of characteristic vibrational modes ($E_1$(TO), $E_1$(LO), $A_1$, and $E_2$) of 2D-Te over treatment time. e) Detailed 2D map of the $A_1$ Raman peak evolution during UV-$O_3$ treatment (0 to 60 min). f) High-frequency region of the Raman spectra, highlighting the emergence of a new peak at 618 $cm^{-1}$, providing evidence for a-$TeO_3$ phase formation.

### 2.2. Structural and Spectroscopic Analyses of 2D-Te During UV-$O_3$ Treatment

**Figure** 2a shows the time-dependent morphological evolution of 2D Te under UV-$O_3$ treatment, which was comprehensively visualized through optical microscopy (OM) and atomic force microscopy (AFM) analyses. These analyses demonstrate progressive surface modification at specific time intervals (0, 10, 30, and 60 min). The OM images clearly reveal a gradual change in optical contrast and surface characteristics, while the corresponding AFM topographical images provide detailed surface morphology information, collectively illustrating the transformation from crystalline 2D-Te to its oxidized state during the UV-$O_3$ treatment process. The quantitative thickness analysis, depicted in Figure 2b, identifies four distinct phases of structural evolution during UV-$O_3$ treatment. In the pristine state (0 min), the 2D Te flakes exhibit an initial thickness of ≈8 nm with uniform surface characteristics. During the early oxidation phase (0-10 min), the flakes maintain their original thickness while forming surface tellurium oxides ($TeO_x$), indicating that the oxidation is initially confined to the surface region. A significant structural transformation occurs in the intermediate phase (30 min), where the thickness substantially increases to 12.8 nm, suggesting the formation of a-$TeO_3$. In the final phase (60 min), further oxidation leads to an additional thickness increase to 13.7 nm, indicating the presence of previously unoxidized 2D-Te layers at the bottom of the flake. Notably, extended treatment beyond 60 min shows negligible thickness variation, confirming the completion of the oxidation process. To establish the thickness-dependent oxidation kinetics, we systematically investigated the UV-$O_3$ treatment effects across a range of 2D-Te samples (5–15 nm). Thin samples (<10 nm) exhibited thickness saturation after 30 min of treatment, while thick samples showed continuous oxidation (Figure S6, Supporting Information). The absorption spectra in Figure 2c reveal that the a-$TeO_3$ formed after 30 min of UV-$O_3$ treatment exhibits an optical bandgap of ≈3 eV (Figure S7, Supporting Information). This represents a significant increase compared to the bandgap of the pristine 2D-Te of 0.35 eV, and notably exceeds the reported bandgap values for $TeO_3$.[21] The substantial bandgap expansion can be attributed to the strong orbital hybridization between O 2p states and the electronic structure of Te during the Te—O bond formation.[22] The fundamental differences in electronic properties between crystalline $\beta$-$TeO_3$ and amorphous a-$TeO_3$, mainly due to the presence of oxygen vacancies and the resulting NBO states, are further discussed in Supporting Information S8. Time-dependent Raman spectroscopy further elucidates the structural transformation during the UV-$O_3$ treatment process (Figure 2d). Raman analysis of crystalline 2D-Te reveals distinct vibrational modes characteristic of its helical chain structure with three well-resolved peaks corresponding to the fundamental phonon modes: $E_1$(TO) at 94.08 $cm^{-1}$, $E_1$(LO) at 106.09 $cm^{-1}$, $A_1$ at 122.77 $cm^{-1}$, and $E_2$ mode at 142.82 $cm^{-1}$. The $A_1$

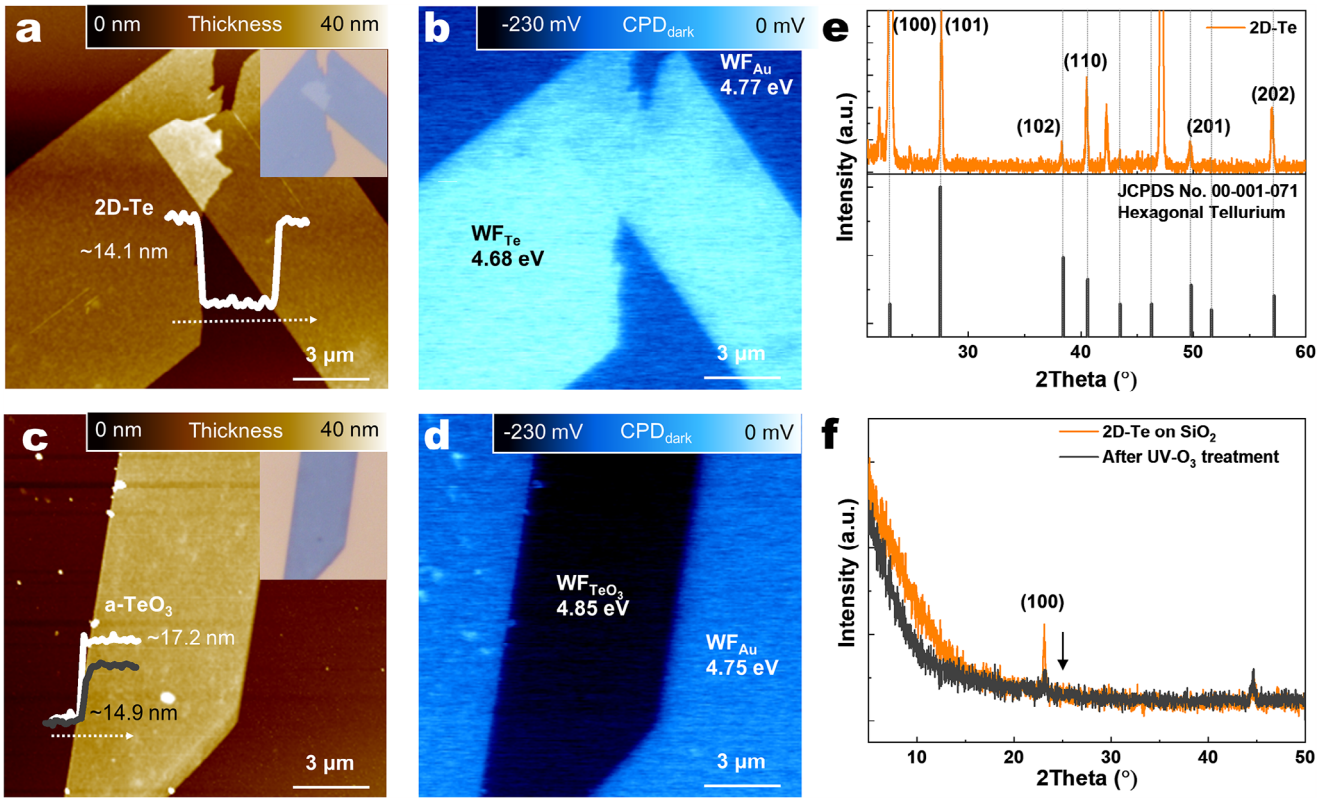


**Figure 3.** a) AFM image of 2D-Te revealing a smooth surface indicative of a highly crystalline and homogeneous structure (white line, 14.1 nm). Inset is OM image b) Contact potential difference (CPD) map of 2D-Te, with the contrast reflecting the difference between the work functions of Au (4.77 eV) and Te (4.68 eV). c) AFM image of a-$TeO_3$ with height profiles showing the initial 2D-Te thickness (black line, 14.9 nm) and thickness after oxidation to a-$TeO_3$ (white line, 17.2 nm). d) CPD map of a-$TeO_3$. e) X-ray diffraction (XRD) pattern of pristine 2D-Te, displaying the typical diffraction peaks of hexagonal Te (JCPDS no. 00-001-071). f) XRD spectra for a 2D-Te film on a $SiO_2$ substrate before (orange) and after 60 min of UV-$O_3$ treatment (gray), showing a notable reduction in the (100) diffraction peak upon oxidation.

mode exhibiting the highest peak intensity, indicates the strong symmetric breathing vibrations of Te atoms within the helical chains. During the first 10 min of UV-$O_3$ treatment, negligible changes in thickness and Raman signals were observed, primarily because the decomposition of surface organics and the presence of a pre-existing $TeO_2$ layer delayed deeper oxidation.[14,23] Notably, after 30 min of treatment, we observe a dramatic decrease in peak intensity accompanied by a significant redshift. As the exposure time increases, the $A_1$ peak undergoes significant broadening and a pronounced red-shift, a characteristic behavior of 2D-Te structures with thicknesses below 5 nm.[13] After 30 min, the observed peak evolution and increased full width at half maximum indicate the presence of pristine ultrathin 2D-Te layers (Figure 2e). The Raman spectra in the 200–520 $cm^{-1}$ range are provided in Figure S9 (Supporting Information). This distinctive spectral behavior serves as a clear indicator of the dimensional transition in the 2D-Te structure, elucidating the formation of atomically thin layers during the degradation process. A newly emerged peak near 618 $cm^{-1}$ (Figure 2f) strongly supports the presence of Te—O bonding, indicative of an amorphous tellurium trioxide (a-$TeO_3$) phase. This assignment is consistent with previously reported Raman analyses of tellurite systems in which characteristic vibrational modes attributed to Te—O bonding appear in the 600–650 $cm^{-1}$ region.[24,25]

### 2.3. Surface Potential and Work Function Analysis

The electronic structure of 2D-Te was thoroughly investigated through AFM and Kelvin probe force microscopy (KPFM) measurements. AFM topography analysis (**Figure 3a**) reveals a uniform thickness of 14.1 nm for the 2D-Te with well-defined boundaries. Contact potential difference (CPD) measurements were utilized to determine the work function (WF) characteristics (Figure 3b). The CPD is defined as the difference in WFs between the tip ($WF_{tip}$) and the sample ($WF_{sample}$), expressed by the equation: $CPD = (WF_{tip} - WF_{sample})/e$, where $e$ is the elementary charge. Through CPD measurements, the WF of the underlying Au substrate was estimated to be 4.77 eV, while 2D-Te exhibited a WF of 4.68 eV. As observed in Figure 3a, the stacked flake configuration of 2D-Te maintains consistent WF values. The consistent WF behavior across different stack configurations suggests that neither the internal electric field generated at the stack interface nor varying 2D-Te thickness affects WF values. This stability in WF across different configurations indicates the robust electronic properties of 2D-Te structures. AFM topography analysis of a-$TeO_3$ reveals a distinct thickness evolution from the initial 2D-Te state (Figure 3c). The thickness increase from 14.9 nm to 17.2 nm after UV-$O_3$ treatment indicates successful amorphization of the 2D-Te. KPFM measurements revealed that

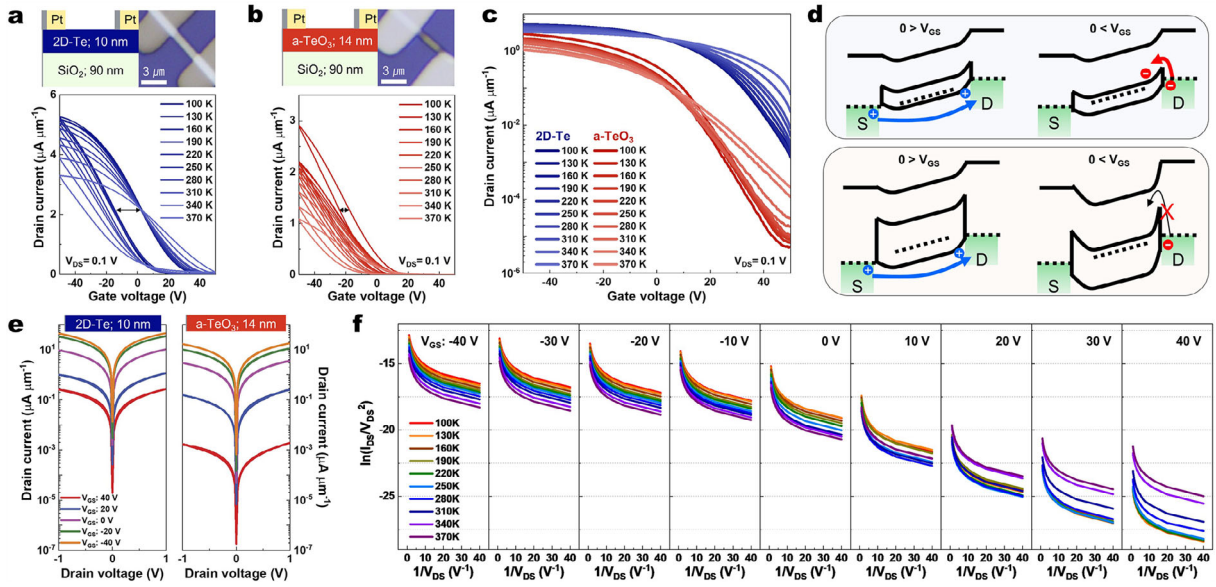


**Figure 4.** a,b) Linear $I_{DS}$-$V_{BG}$ of 2D-Te (10 nm, blue) and a-$TeO_3$ (14 nm, red) transistors measured from 100 K to 370 K at $V_{DS} = 0.1$ V, showing reduced hysteresis in a-$TeO_3$ transistors. c) Logarithmic-scale $I_{DS}$-$V_{BG}$ measured from 100 K to 370 K at $V_{DS} = 0.1$ V, highlighting superior on/off characteristics of a-$TeO_3$ transistor. d) The band diagrams compare the carrier transport mechanisms in 2D-Te (top) and a-$TeO_3$ (bottom) under different gate voltage conditions. Under negative gate bias ($0 > V_{BG}$), both materials exhibit hole accumulation in the channel, with a-$TeO_3$ demonstrating stronger on-state characteristics. Under positive gate bias ($0 < V_{BG}$), 2D-Te shows some electron transport due to its smaller bandgap, while a-$TeO_3$ effectively blocks electron flow due to its wider bandgap, as indicated by the "X" symbol. e) Logarithmic-scale $I_{DS}$-$V_{DS}$ sweep results of 2D-Te (10 nm) and a-$TeO_3$ (14 nm) transistors measured with $V_{DS}$ sweeping from -1 V to 1 V under various gate voltages ($V_{BG} = -40$ V (orange) to 40 V (red), step = 20 V). Both transistors exhibit clear ohmic behavior. f) FN tunneling plot for a-$TeO_3$ transistors at $V_{DS} = 1$ V, showing two distinct operating conditions: $V_{BG} = 40$ V (off-state, right) and $V_{BG} = -40$ V (on-state, left).

the Au reference electrode maintained a WF of 4.75 eV, while a-$TeO_3$ exhibited an enhanced WF of 4.85 eV (Figure 3d). Compared to pristine 2D-Te, a-$TeO_3$ shows a significant WF difference ($\Delta\Phi$) of 0.17 eV, indicating fundamental modifications in the electronic structure following amorphization. This substantial electronic transformation is further validated through comprehensive band structure, detailed in Figure S10 (Supporting Information), which provides insights into the electronic reconfiguration mechanism of a-$TeO_3$. The X-ray diffraction (XRD) pattern of pristine 2D-Te shows a clear hexagonal crystal structure with major diffraction peaks closely matching the standard references for $\beta$-Te. In particular, the (100) plane shows a clear and prominent signal, highlighting the well-defined crystallinity of the synthesized 2D-Te (Figure 3e). Figure 3f shows the XRD pattern after 60 min of UV-$O_3$ exposure, where the (100) peak shows a significant decrease in intensity. This marked decrease indicates that the oxidation-driven amorphization process is progressing over time, leading to the gradual loss of the crystalline peaks observed in the pristine state.

### 2.4. Carrier Transport Mechanisms in P-channel Field Effect Transistors

The comparative analysis of linear transfer characteristics between 2D-Te and a-$TeO_3$-based transistors reveals striking differences in their hysteresis behavior across the temperature range of 100–370 K. As shown in **Figure** 4a,b, the forward and backward voltage sweeps demonstrate significantly reduced hysteresis in a-$TeO_3$ transistors compared to 2D-Te structures. The a-$TeO_3$ device continues to operate normally after four months in air, demonstrating its robust air stability (Figure S11, Supporting Information). The trap charge density, calculated as $N_T = Q_m/q$, where $Q_m$ represents the mobile charge density obtained from temperature-dependent hysteresis measurements (Figure S12, Supporting Information), shows that a-$TeO_3$ transistors exhibit a notably lower trap density ($2.69 \times 10^{14}$ $cm^{-2}$) compared to 2D-Te ($6.50 \times 10^{14}$ $cm^{-2}$). This substantial reduction in interface-induced hysteresis is particularly evident in the linear transfer curves, where a-$TeO_3$ exhibits more consistent temperature-dependent behavior. At $V_{DS} = 0.1$ V, the a-$TeO_3$-based transistor (14 nm) demonstrates remarkably improved interface characteristics with a maximum drain current of ≈3 μA $\mu m^{-1}$ and sharper switching characteristics, while the 2D-Te-based transistor (10 nm) shows a higher maximum current of 5 μA $\mu m^{-1}$ but with more gradual slope changes. Temperature-dependent measurements conducted from 100 to 370 K further highlight the superior performance of a-$TeO_3$ transistors. These devices maintain excellent interface quality and stable operating characteristics throughout the entire temperature range. The enhanced performance can be primarily attributed to the improved interface between a-$TeO_3$ and the 90 nm $SiO_2$ layer. The oxidized state of a-$TeO_3$ leads to better compatibility with $SiO_2$, resulting in a reduced density of interface states and more efficient carrier transport mechanisms. Figure 4c presents logarithmic-scale transfer curves ($I_{DS}$-$V_{BG}$) measured from 100 to 370 K at $V_{DS} = 0.1$ V, revealing distinct transport behaviors. In particular, the a-$TeO_3$ transistor exhibits superior on/off characteristics with an exceptionally low off-state

current of $10^{-5}$ μA μm$^{-1}$ compared to 2D-Te. This phenomenon can be explained by the band transport diagrams (Figure 4d), where the wider bandgap of a-$TeO_3$ provides effective potential barriers to carrier transport modulation. Under positive gate bias conditions ($V_{BG} > 0$), the elevated barrier height substantially impedes electron transport, resulting in the observed superior off-state characteristics. Figure 4e presents logarithmic-scale output characteristics ($I_{DS}$-$V_{DS}$) of both 2D-Te (10 nm) and a-$TeO_3$ (14 nm) transistors measured with $V_{DS}$ sweeping from −1 to 1 V under various gate voltages ($V_{BG}$ = −40–40 V). Both transistors, fabricated on the same flake, exhibit clear Ohmic behavior in the low-bias regime, indicating good metal-semiconductor contact properties. The systematic modulation of drain current with gate voltage demonstrates effective electrostatic control in both cases. However, their response to electrical field modulation via back-gate control shows distinct differences. The 2D-Te transistor demonstrates a moderate on/off current ratio of ≈$10^2$ at $V_{DS} = 0.1$ V, while the a-$TeO_3$ transistor achieves a significantly enhanced ratio of ≈$10^5$ at the same $V_{DS}$. In this study, the a-$TeO_3$ layer was prepared from 2D-Te samples with a thickness of 10–15 nm by UV-$O_3$ treatment. Among them, the 14 nm sample showed the best performance in terms of on/off current ratio, mobility and threshold voltage. Comparative graphs of FET characteristics based on thickness variations are presented in Figure S13 (Supporting Information). At the metal-semiconductor interface, carrier transport is typically governed by three primary mechanisms: direct tunneling, Fowler-Nordheim (FN) tunneling, and thermionic emission. In the a-$TeO_3$-based transistors, the high intrinsic carrier concentration leads to the dominance of FN tunneling, even at low $V_{DS}$ of 1 V (Figure 4f). This predominant FN tunneling behavior at such low bias conditions underscores the unique electronic properties of a-$TeO_3$, where the elevated carrier density significantly modifies the interfacial transport characteristics. Electrical characterization conducted at a $V_{BG}$ of 40 V demonstrates a pronounced temperature-dependent behavior in the carrier transport. The measured current at 100 K exhibits notably lower values compared to 370 K, indicating carrier injection limitations due to insufficient thermal energy. This behavior demonstrates the simultaneous presence of FN tunneling and thermionic emission as primary transport mechanisms. The off state of the transistor can be distinctly identified through the divergence between 100 K and 370 K curves in the FN plot. When the gate bias is shifted to -40 V, where hole accumulation becomes prominent, an intriguing temperature inversion phenomenon is observed. The current at 100 K surpasses that at 370 K, which can be attributed to enhanced FN tunneling resulting from increased hole concentration (majority carriers). The unique identification of the transistor off-state, characterized by the divergence in temperature-dependent FN plots, is consistently observed across various 2D-Te transistors (Figure S14, Supporting Information).

### 2.5. Temperature and Gate Voltage-Dependent Mobility Characteristics

The temperature and gate voltage-dependent mobility characteristics reveal distinct material-specific behaviors between 2D-Te and a-$TeO_3$, as evidenced in their respective 2D mapping profiles. **Figure 5a** shows that crystalline 2D-Te displays a significant decrease in mobility as the electric field increases. This reduction in mobility is attributed to enhanced impurity scattering effects at higher electric fields. A notable mobility peak is observed near $V_{BG} = 0$ V, attributed to maximum transconductance in this region. In contrast, a-$TeO_3$ (Figure 5b) exhibits distinctly disparate behavior, displaying an unexpected increase in mobility under high electric field conditions ($V_{BG}$ = −50 V, E = −4.44 MV). This phenomenon can be effectively explained through Matthiessen's rule ($1/\mu_{total} = 1/\mu_{lattice} + 1/\mu_{impurity}$).[26] The inherently low carrier concentration in a-$TeO_3$ results in reduced susceptibility to impurity scattering, even under high electric field conditions. Detailed analysis of the slope variations due to reduced phonon scattering in the maximum mobility region is provided in Figure S15 (Supporting Information). Under high electric field conditions, temperature-dependent mobility measurements (Figure 5c) reveal superior performance of a-$TeO_3$ compared to 2D-Te. This enhanced mobility in a-$TeO_3$ can be attributed to its wider bandgap and lower charge carrier density, which significantly reduces the impact of impurity scattering, particularly at low temperatures. Furthermore, as shown in Figure 5d, a-$TeO_3$ achieves remarkable on/off ratios exceeding $10^5$ at low temperatures, effectively addressing the limitations of 2D-Te in p-channel transistor applications, which are primarily due to its high electron density and narrow bandgap. In order to verify the full conversion of the channel layer to a-$TeO_3$, it is crucial that no further increases in thickness or changes in electrical properties are observed after the initial 60-min UV-$O_3$ treatment, even with additional UV-$O_3$ exposure. The results of the extended UV-$O_3$ treatment are shown in Figure S16 (Supporting Information).

### 2.6. Comparative Transistor Performance Metrics of Contact Resistance and P-channel Transistor

The fundamental charge transport mechanisms at the interface between platinum (Pt) contacts and our semiconductor materials (2D-Te and a-$TeO_3$) were thoroughly investigated through temperature-dependent electrical measurements. **Figure 6a** presents the Richardson plot analysis, which is derived from the thermionic emission theory described by the equation[27]

$$I_{DS} = WA_{2D}^{*}T^{\frac{3}{2}}exp\left(-\frac{\Phi_B}{k_BT}\right)\left[1-exp\left(\frac{-qV_{DS}}{k_BT}\right)\right], A_{2D}^{*} = \frac{q\sqrt{8\pi {k_B}^3 m^*}}{h^2} \quad (1)$$

where $W$ represents the channel width, $A_{2D}^{*}$ is the modified Richardson constant for a 2D semiconductor, $T$ is the temperature, $k_B$ is the Boltzmann constant, q is the electron charge, $m^*$ is the effective mass, $h$ is the Planck constant, and $\Phi_B$ denotes the SBH. The data is plotted as $\ln(I_{DS}/T^{3/2})$ versus 1000/T under various $V_{BG}$ ranging from −40 to +40 V. We used the $T^{3/2}$ dependence in our thermionic emission calculations based on these theoretical and experimental findings. Recent studies have demonstrated that the thermionic emission characteristics of 2D materials continue to be predominantly governed by their intrinsic electronic

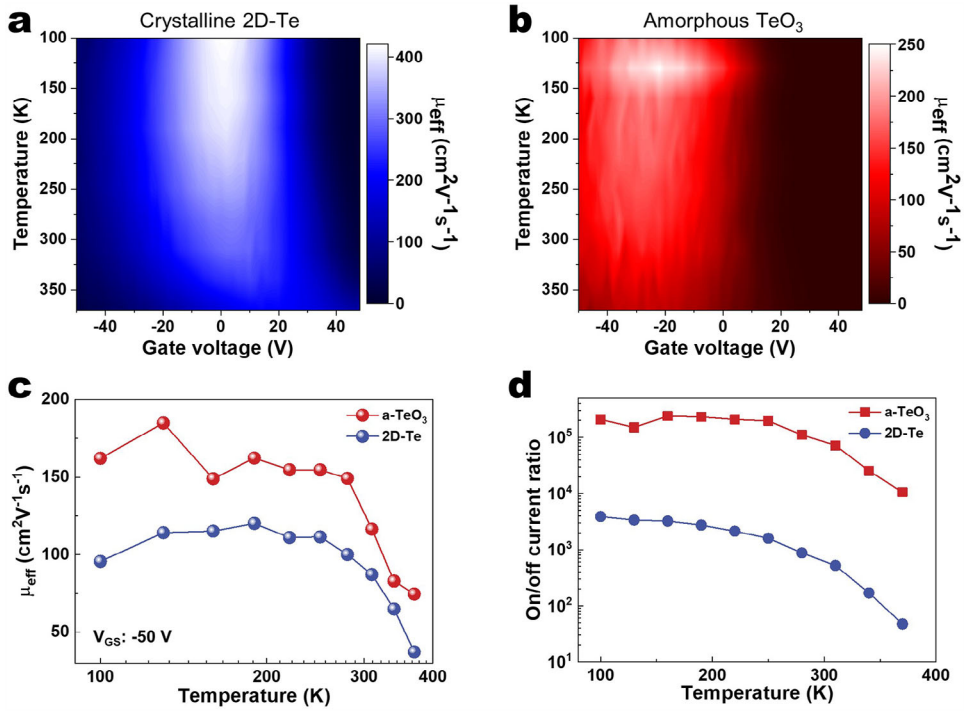


**Figure 5.** a) 2D color map illustrating the temperature-dependent transfer characteristics of 2D-Te (blue), and b) a-$TeO_3$ (red). The x-axis represents the gate voltage ranging from −50 to 50 V, while the y-axis displays the temperature scale from 100 K to 370 K. c) Field-effect mobility as a function of temperature for both a-$TeO_3$ (red) and 2D-Te (blue) at high gate bias ($V_g$ = -50 V). d) Temperature-dependent on/off current ratio comparison between a-$TeO_3$ (red) and 2D-Te (blue).

structure, even in amorphous states.[28,29] Based on these findings, we hypothesized that the thermionic emission properties of our 2D-Te and a-$TeO_3$ samples would also reflect their distinct electronic structures despite the presence of structural disorder. The linear behavior observed in these Arrhenius plots confirms that thermionic emission is the dominant transport mechanism, with the slope of each line directly proportional to the SBH ($-q\Phi_B/k$). The systematic shift in these curves with varying gate voltages demonstrates the effective modulation of the SBH at the metal-semiconductor interface. Figure 6b presents a detailed analysis of the SBH as a function of gate voltage for both 2D-Te and a-$TeO_3$ materials, measured at two distinct flat-band voltages ($V_{FB}$ = 5.05 V and 30.08 V). The results reveal a remarkable contrast: crystalline 2D-Te exhibits a substantial barrier height of 73 meV, while a-$TeO_3$ demonstrates an exceptionally low barrier of 10 meV when in contact with Pt ($\Phi_{M,Pt} \approx 5.65$ eV). Figure 6c illustrates the band alignment diagrams at the Pt/semiconductor interface for both materials, highlighting the fundamental differences in Fermi level pinning (FLP) behavior.[30] The crystalline 2D-Te shows the FLP effect, characterized by rigid band alignment and significant band bending at the interface. In contrast, a-$TeO_3$ exhibits weak FLP, demonstrated by its remarkably low SBH of 10 meV. The low SBH in a-$TeO_3$ results from multiple interface effects rather than just orbital hybridization between Pt d-orbitals and oxygen 2p orbitals.[31,32] The amorphous structure could create favorable conditions through disorder effects and oxygen-related defect states, leading to modified interface electronic properties.[33,34] Figure 6d-f demonstrates the exceptional electrical characteristics and potential applications of our a-$TeO_3$-based transistors. The $R_c$ and sheet resistance ($R_s$) characteristics were systematically investigated as a function of gate voltage (Figure 6d). As the gate voltage increases from −10 to −40 V, both the $R_c$ and sheet resistance show a decreasing trend, with $R_c$ reducing from 0.70 to 0.62 kΩ·μm and $R_s$ decreasing from 1.91 to 1.02 kΩ/sq. Detailed electrical measurements of transistors with various channel lengths using the transfer length method are provided in Figure S17 (Supporting Information). These notably low $R_c$ values, coupled with reduced sheet resistance, can be attributed to the high carrier concentration and correlate well with the observed weak FLP at the Pt contact interface. In the broader context of 2D materials and their contact properties, our a-$TeO_3$ transistor demonstrates remarkable performance metrics (Figure 6e). When comparing the $R_c$ against carrier density ($n_{2D}$), our work positions itself advantageously near the quantum limit, outperforming various established 2D material systems including Pt/$MoTe_2$, Co/hBN/$MoS_2$, Bi/$MoS_2$ and conventional metal-semiconductor interfaces.[35–42] The transistor performance metrics illustrated in Figure 6f present a comprehensive comparison of on/off current ratios versus effective hole mobility across various p-channel transistors, incorporating both 2D materials and 3D oxide semiconductors. The 14 nm a-$TeO_3$ transistor exhibited a remarkable hole mobility of 238.6 $cm^2\ V^{-1}s^{-1}$ with an exceptional on/off current ratio of $0.81 \times 10^5$, while the 10 nm 2D-Te transistor achieved an even higher mobility of 371.1 $cm^2\ V^{-1}\ s^{-1}$ with an on/off ratio of $1.47 \times 10^2$. Detailed mobility extraction can be found in Figure S18 (Supporting Information), which also shows the results of the $n_{2D}$ calculations.[4,13,37,43–60] Notably, these remarkable performance metrics were achieved using a relatively

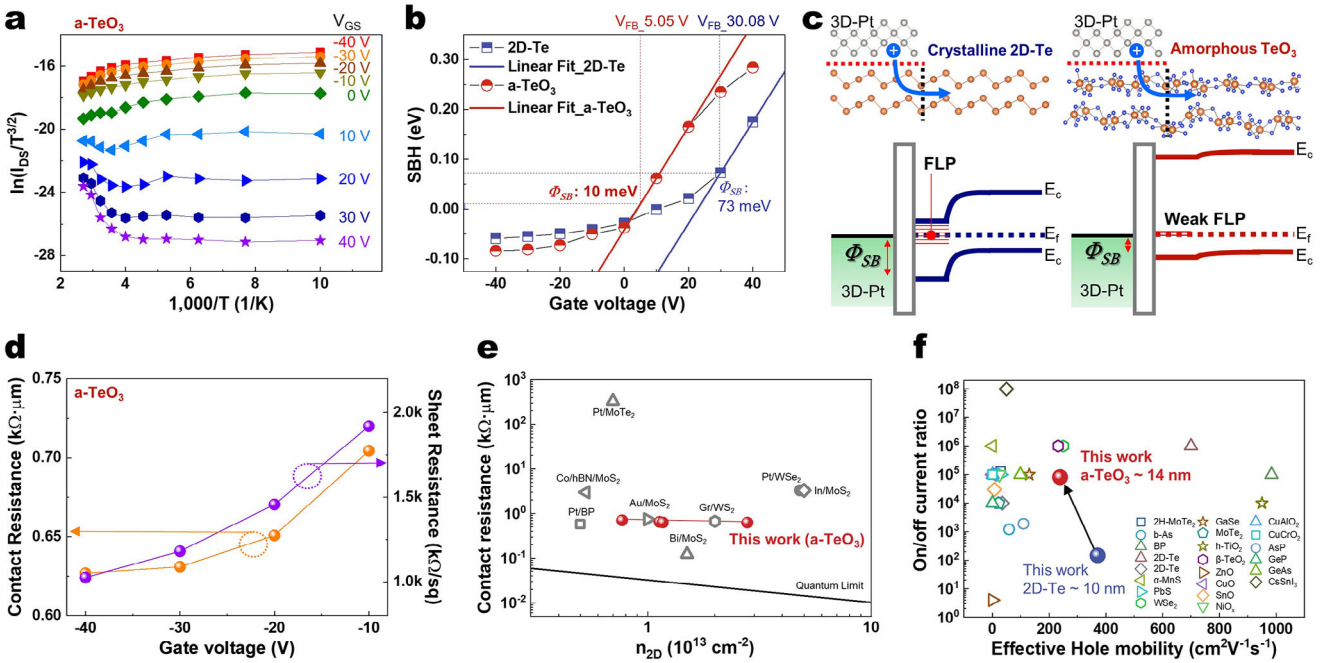


**Figure 6.** a) Richardson plot analysis ($\ln(I_{DS}/T^{3/2})$ vs. 1,000/T) for the Pt/a-$TeO_3$ interface, with gate voltages ranging from −40 V (red) to 40 V (purple) in 10 V steps. This plot demonstrates thermionic emission as the dominant transport mechanism at the metal-semiconductor interface. b) SBH as a function of gate voltage for 2D-Te and a-$TeO_3$, measured at flat-band voltages of 5.05 and 30.08 V. 2D-Te shows a high SBH of 73 meV, while a-$TeO_3$ exhibits a remarkably low SBH of 10 meV when in contact with Pt ($\Phi_{M,Pt} \approx 5.65$ eV). c) Band alignment diagrams illustrating FLP in 2D-Te (left) and weak FLP in a-$TeO_3$ (right). The diagram emphasizes the weakened FLP at the interface between a-$TeO_3$ and 3D Pt contacts. d) $R_c$ (orange) and $R_s$ (purple) as a function of gate voltage for a-$TeO_3$, showing decreasing trends with increasing negative gate voltage. e) Comparison of contact resistance vs. carrier density ($n_{2D}$) for various 2D material systems, highlighting the superior performance of a-$TeO_3$ near the quantum limit.[35–42] f) On/off current ratio vs. effective hole mobility for p-channel transistors based on 2D materials and 3D oxide semiconductors. The 14 nm a-$TeO_3$ transistor shows a mobility of 238.6 $cm^2\ V^{-1}\ s^{-1}$ with an on/off ratio of $0.81 \times 10^5$, while the 10 nm 2D-Te transistor achieves 371.1 $cm^2\ V^{-1}\ s^{-1}$ mobility with an on/off ratio of $1.47 \times 10^2$.[4,5,13,37,43–60]

low-$\kappa$ $SiO_2$ dielectric layer ($\kappa \approx 3.9$) with a thickness of 90 nm as the gate insulator. This achievement is particularly significant as it suggests substantial room for further performance enhancement through optimization of the gate stack, such as implementing high-$\kappa$ dielectric materials or reducing substrate phonon scattering and charge impurity effects via hexagonal boron nitride encapsulation.

## 3. Conclusion

Through comprehensive electrical measurements conducted across various temperatures and applied electric fields, we demonstrate the first realization of a-$TeO_3$ as a high-performance p-channel semiconductor via controlled UV-$O_3$ treatment of 2D-Te. The phase transformation induces dramatic bandgap widening, effectively overcoming the inherent limitations of 2D-Te while preserving its advantageous carrier transport properties. Our findings reveal that, remarkably, despite the use of 3D-Pt contacts, a-$TeO_3$ exhibits exceptionally low SBH and weak Fermi level pinning at the contact interface, enabling superior contact characteristics. The widened bandgap not only ensures stable switching characteristics but also enhances environmental stability under ambient conditions. Most significantly, the unique electronic structure of a-$TeO_3$ facilitates exceptional field-effect transistor performance, combining high hole mobility with excellent on/off characteristics. The carrier transport mechanism is predominantly governed by FN tunneling and thermionic emission. A distinct mobility inversion phenomenon occurs at low temperatures when gate bias fields exceed −40 V. Under these conditions, a-$TeO_3$ demonstrates superior mobility compared to 2D-Te. This behavior can be attributed to the semimetal-like high carrier concentration in 2D-Te. These results not only establish a-$TeO_3$ as a promising platform for next-generation p-channel transistors but also open new possibilities for phase engineering in high-performance semiconductor development.

## 4. Experimental Section

*Phase Transformation of 2D-Te to a-$TeO_3$*: The controlled oxidation of 2D-Te was performed using a UV-Ozone treatment system (Ossila) equipped with a dual-wavelength mercury lamp source. The system utilizes two distinct UV wavelengths: 185 nm (646 kJ $mol^{-1}$) and 254 nm (472 kJ $mol^{-1}$). The 185 nm radiation generates ozone by interacting with atmospheric oxygen, while the 254 nm radiation facilitates both ozone decomposition and surface oxidation processes. The phase transformation mechanism was primarily driven by the high-energy UV photons, particularly at 254 nm (472 kJ $mol^{-1}$), which significantly exceeds the electron affinity of Te (190.02 kJ $mol^{-1}$). This energy difference enables efficient electron excitation and subsequent oxidation reactions, promoting the transformation of 2D-Te to a-$TeO_3$. The simultaneous presence of ozone,

generated by the 185 nm radiation, further enhances the oxidation process through reactive oxygen species formation (Figure S19, Supporting Information).

*Fabrication of a-$TeO_3$ Transistor*: The crystalline 2D-Te was synthesized via the hydrothermal method.[13] All transistors were fabricated on a 90 nm $SiO_2$ dielectric layer. The source and drain electrodes were patterned using photolithography, followed by sputter deposition of 50 nm platinum (Pt). To ensure consistent performance comparison, all transistors were fabricated using wire-like crystalline 2D-Te with fixed dimensions of 3.49 µm in length and 0.78 µm in width. Multiple transistors were fabricated and characterized to verify the reproducibility of the electrical measurements.

*Transistor Characterization*: The electrical properties were measured using a vacuum probe system (model 4200, Keithley) in a low-vacuum environment ($10^{-3}$ Torr). All measurements were performed with normal sweep delay settings, and the transfer characteristics were obtained by sweeping the gate voltage from 0 V in the sequence of off state → on state → off state to ensure comprehensive transistor characterization.

*KPFM Measurements*: The surface topography and contact potential difference (CPD) maps were obtained using an atomic force microscope (NX10, Park Systems) equipped with a glove box. The measurements were performed in a $N_2$ atmosphere to minimize environmental artifacts. The 2D-Te and a-$TeO_3$ samples were prepared on Au substrates, and all measurements were conducted under dark conditions. NSG01/Pt-coated cantilevers (NT-MDT) were used as the probe tip, with scan parameters set to 15 × 15 µm$^2$ (256 × 256 pixels) at a scan rate of 0.35 Hz. The work function was calibrated using a highly ordered pyrolytic graphite (HOPG, SPI suppliers) reference sample.

*HRTEM Analysis*: TEM measurements were conducted at an acceleration voltage of 200 kV. Cross-sectional specimens of 43-nm-thick UV-$O_3$ treated (60 min) samples were prepared by focused ion beam milling. The microscope, equipped with high-angle annular dark-field scanning transmission electron microscopy capability, revealed the formation of a-$TeO_3$ phase from the surface of the UV-$O_3$ treated samples.

*XPS Measurements*: XPS analysis was conducted using a Theta Probe spectrometer (Thermo Fisher Scientific) equipped with a monochromatic Al K$\alpha$ source ($h\nu$ = 1486.7 eV, resolution: 0.85 eV) under ultra-high vacuum conditions ($10^{-9}$ Torr). High-resolution spectra were acquired at a 90° take-off angle with 100 eV pass energy and 50 ms dwell time per step. Peak deconvolution was performed using Thermo Avantage software after smart background subtraction.

*Confocal Raman spectroscopy*: Raman measurements were performed using a Horiba LabRAM HR Evolution confocal microscope with a 532 nm linearly polarized laser source. The laser beam was focused through a 100× Olympus objective (NA = 0.9), with the excitation power maintained at 220 µW to prevent sample damage. The scattered light was analyzed using a spectrometer equipped with an 1800 g/mm grating and a charge-coupled device detector, achieving a spectral resolution of 0.6 cm$^{-1}$. Measurements were systematically conducted with incrementally increased acquisition times to ensure optimal signal quality and reproducibility.

*High-Resolution XRD*: HR-XRD measurements were performed using a Rigaku SmartLab diffractometer equipped with a Cu K$\alpha$ radiation source. Diffraction patterns were obtained over a 2$\theta$ range of 20–60° and 5–50°. The X-ray tube was operated at an accelerating voltage between 20 and 60 kV.

## Supporting Information

Supporting Information is available from the Wiley Online Library or from the author.

## Acknowledgements

S.B. and C.L. contributed equally to this work. This research was supported by the Basic Science Research Program through the National Research Foundation of Korea (NRF) funded by the Ministry of Education (RS-2023-00245971). It was also supported by NRF grants funded by the Korean government (MSIT) (RS-2023-00260527, RS-2024-00341837, and 2022R1A2C2091945).

## Conflict of Interest

The authors declare no conflict of interest.

## Data Availability Statement

The data that support the findings of this study are available from the corresponding author upon reasonable request.

## Keywords

amorphous oxide semiconductor, oxidation, p-channel transistor, structural transformation, tellurium trioxide

Received: March 13, 2025
Revised: May 24, 2025
Published online: June 16, 2025

[1] S. Wang, X. Liu, P. Zhou, *Adv. Mater.* **2022**, *34*, 2106886.
[2] A. Liu, Y.-S. Kim, M. G. Kim, Y. Reo, T. Zou, T. Choi, S. Bai, H. Zhu, Y.-Y. Noh, *NatureNature* **2024**, *629*, 798.
[3] A. Oberoi, Y. Han, S. P. Stepanoff, A. Pannone, Y. Sun, Y.-C. Lin, C. Chen, J. R. Shallenberger, D. Zhou, M. Terrones, J. M. Redwing, J. A. Robinson, D. E. Wolfe, Y. Yang, S. Das, *ACS Nano* **2023**, *17*, 19709.
[4] L. Li, Y. Yu, G. J. Ye, Q. Ge, X. Ou, H. Wu, D. Feng, X. H. Chen, Y. Zhang, *Nat. Nanotechnol.* **2014**, *9*, 372.
[5] H. Fang, S. Chuang, T. C. Chang, K. Takei, T. Takahashi, A. Javey, *Nano Lett.* **2012**, *12*, 3788.
[6] Z. Wang, H. Xia, P. Wang, X. Zhou, C. Liu, Q. Zhang, F. Wang, M. Huang, S. Chen, P. Wu, Y. Chen, J. Ye, S. Huang, H. Yan, L. Gu, J. Miao, T. Li, X. Chen, W. Lu, P. Zhou, W. Hu, *Adv. Mater.* **2021**, *33*, 2104942.
[7] S. Bang, W. Kang, D. Kim, H. C. Suh, D. H. Kim, C. Kwon, J. Jo, J. Kim, H. Ko, K. K. Kim, J. Ahn, M. S. Jeong, *Nano Lett.* **2024**, *24*, 9889.
[8] S. Bang, S. Lee, A. Rai, N. T. Duong, I. Kawk, S. Wolf, C. Chung, S. K. Banerjee, A. C. Kummel, M. S. Jeong, J. H. Park, *Adv. Funct. Mater.* **2020**, *30*, 2000250.
[9] J. Lee, S. Bang, H. J. Park, D. Y. Park, C. Park, N. T. Duong, Y. S. Won, J. Jang, H. M. Oh, S. H. Choi, K. K. Kim, M. S. Jeong, *ACS Appl. Mater. Interfaces* **2021**, *13*, 55489.
[10] E. Fortunato, P. Barquinha, R. Martins, *Adv. Mater.* **2012**, *24*, 2945.
[11] H. Kawazoe, H. Yanagi, K. Ueda, H. Hosono, *MRS Bull.* **2000**, *25*, 28.
[12] A. Liu, H. Zhu, W.-T. Park, S.-J. Kim, H. Kim, M.-G. Kim, Y.-Y. Noh, *Nat. Commun.* **2020**, *11*, 4309.
[13] Y. Wang, G. Qiu, R. Wang, S. Huang, Q. Wang, Y. Liu, Y. Du, W. A. Goddard, M. J. Kim, X. Xu, P. D. Ye, W. Wu, *Nat. Electron.* **2018**, *1*, 228.
[14] X. Zheng, Y. Wei, C. Deng, H. Huang, Y. Yu, G. Wang, G. Peng, Z. Zhu, Y. Zhang, T. Jiang, S. Qin, R. Zhang, X. Zhang, *ACS Appl. Mater. Interfaces* **2018**, *10*, 30045.
[15] Z. Shi, R. Cao, K. Khan, A. K. Tareen, X. Liu, W. Liang, Y. Zhang, C. Ma, Z. Guo, X. Luo, H. Zhang, *Nano-Micro Lett.* **2020**, *12*, 99.
[16] S. Li, H. Zhang, H. Ruan, Z. Cheng, Y. Yao, F. Zhuge, T. Zhai, *Adv. Funct. Mater.* **2023**, *33*, 2211527.
[17] C. W. Siders, A. Cavalleri, K. Sokolowski-Tinten, C. Tóth, T. Guo, M. Kammler, M. H. V. Hoegen, K. R. Wilson, D. V. D. Linde, C. P. J. Barty, *ScienceScience* **1999**, *286*, 1340.

[18] H. Zhang, S. Liu, A. Zheng, P. Wang, Z. Zheng, Z. Wang, H. Cheng, Y. Dai, B. Huang, Y. Liu, *Angew. Chem.* **2024**, *136*, 202400965.
[19] C. M. Smyth, G. Zhou, A. T. Barton, R. M. Wallace, C. L. Hinkle, *Adv. Mater. Interfaces* **2021**, *8*, 2002050.
[20] S. Ahmad Kamil, J. Chandrappan, J. Portoles, P. Steenson, G. Jose, *Mater. Res. Express* **2019**, *6*, 086220.
[21] T. Kim, C. H. Choi, P. Byeon, M. Lee, A. Song, K.-B. Chung, S. Han, S.-Y. Chung, K.-S. Park, J. K. Jeong, *Npj 2D Mater. Appl.* **2022**, *6*, 4.
[22] E. M. Roginskii, M. B. Smirnov, V. G. Kuznetsov, O. Noguera, J. Cornette, O. Masson, P. Thomas, *Mater. Res. Express* **2019**, *6*, 125903.
[23] C. Theotis, J. D. Ruiz, H. Fan, C. J. Brinker, B. I. Swanson, A. N. Parikh, *Chem. Mater.* **2000**, *12*, 3879.
[24] S. Altaf, H. Ijaz, J. Haider, M. Naz, M. Aqeel, A. Ul-Hamid, M. Ikram, S. Zulfiqar, S. A. Ditta, A. Shahbaz, M. Ikram, *Appl. Nanosci.* **2020**, *10*, 4241.
[25] T. Sekiya, N. Mochida, A. Soejima, *J. Non-Cryst. Solids* **1995**, *191*, 115.
[26] F. Zhuo, J. Wu, B. Li, M. Li, C. L. Tan, Z. Luo, H. Sun, Y. Xu, Z. Yu, *Research* **2023**, *6*, 0057.
[27] S. B. Mitta, M. S. Choi, A. Nipane, F. Ali, C. Kim, J. T. Teherani, J. Hone, W. J. Yoo, *2D Mater.* **2021**, *8*, 012002.
[28] H. Jang, H. Kim, G. Kim, S. Cho, H. Yang, *Nano Converg.* **2024**, *11*, 46.
[29] Z. Yang, J. Hao, S. P. Lau, *J. Appl. Phys.* **2020**, *127*, 220901.
[30] X. Liu, M. S. Choi, E. Hwang, W. J. Yoo, J. Sun, *Adv. Mater.* **2022**, *34*, 2108425.
[31] J. Zeng, D. He, J. Qiao, Y. Li, L. Sun, W. Li, J. Xie, S. Gao, L. Pan, P. Wang, Y. Xu, Y. Li, H. Qiu, Y. Shi, J.-B. Xu, W. Ji, X. Wang, *Nat. Commun.* **2023**, *14*, 324.
[32] Y. Hu, D. Schlom, S. Datta, K. Cho, *J. Mater. Chem. C* **2023**, *11*, 4830.
[33] K. Auewattanapun, J. P. S. Bermundo, U. Hanifah, H. Nakajima, W. Limphirat, R. Techapiesancharoenkij, Y. Uraoka, *ACS Appl. Mater. Interfaces* **2024**, *16*, 60521.
[34] Y. Zheng, J. Gao, C. Han, W. Chen, *Cell Rep. Phys. Sci.* **2021**, *2*, 100298.
[35] F. Telesio, G. L. Gal, M. Serrano-Ruiz, F. Prescimone, S. Toffanin, M. Peruzzini, S. Heun, *NanotechnologyNanotechnology* **2020**, *31*, 334002.
[36] Y. Wang, J. C. Kim, Y. Li, K. Y. Ma, S. Hong, M. Kim, H. S. Shin, H. Y. Jeong, M. Chhowalla, *NatureNature* **2022**, *610*, 61.
[37] S. Song, A. Yoon, S. Jang, J. Lynch, J. Yang, J. Han, M. Choe, Y. H. Jin, C. Y. Chen, Y. Cheon, J. Kwak, C. Jeong, H. Cheong, D. Jariwala, Z. Lee, S.-Y. Kwon, *Nat. Commun.* **2023**, *14*, 4747.
[38] P.-C. Shen, C. Su, Y. Lin, A.-S. Chou, C.-C. Cheng, J.-H. Park, M.-H. Chiu, A.-Y. Lu, H.-L. Tang, M. M. Tavakoli, G. Pitner, X. Ji, Z. Cai, N. Mao, J. Wang, V. Tung, J. Li, J. Bokor, A. Zettl, C.-I. Wu, T. Palacios, L.-J. Li, J. Kong, *NatureNature* **2021**, *593*, 211.
[39] Y. Wang, J. C. Kim, R. J. Wu, J. Martinez, X. Song, J. Yang, F. Zhao, A. Mkhoyan, H. Y. Jeong, M. Chhowalla, *NatureNature* **2019**, *568*, 70.
[40] X. Cui, E.-M. Shih, L. A. Jauregui, S. H. Chae, Y. D. Kim, B. Li, D. Seo, K. Pistunova, J. Yin, J.-H. Park, H.-J. Choi, Y. H. Lee, K. Watanabe, T. Taniguchi, P. Kim, C. R. Dean, J. C. Hone, *Nano Lett.* **2017**, *17*, 4781.
[41] C. D. English, G. Shine, V. E. Dorgan, K. C. Saraswat, E. Pop, *Nano Lett.* **2016**, *16*, 3824.
[42] C.-H. Yeh, W. Cao, A. Pal, K. Parto, K. Banerjee, in 2019 IEEE Int. Electron Devices Meet. IEDM, IEEE, San Francisco, CA, USA, **2019**.
[43] M. Zhong, Q. Xia, L. Pan, Y. Liu, Y. Chen, H. Deng, J. Li, Z. Wei, *Adv. Funct. Mater.* **2018**, *28*, 1802581.
[44] C. Zhao, C. Tan, D.-H. Lien, X. Song, M. Amani, M. Hettick, H. Y. Y. Nyein, Z. Yuan, L. Li, M. C. Scott, A. Javey, *Nat. Nanotechnol.* **2020**, *15*, 53.
[45] N. Li, Y. Zhang, R. Cheng, J. Wang, J. Li, Z. Wang, M. G. Sendeku, W. Huang, Y. Yao, Y. Wen, J. He, *ACS Nano* **2019**, *13*, 12662.
[46] P. Giraud, B. Hou, S. Pak, J. I. Sohn, S. Morris, S. Cha, J. M. Kim, *NanotechnologyNanotechnology* **2018**, *29*, 075202.
[47] Q. Zhang, X.-F. Wang, S.-H. Shen, Q. Lu, X. Liu, H. Li, J. Zheng, C.-P. Yu, X. Zhong, L. Gu, T.-L. Ren, L. Jiao, *Nat. Electron.* **2019**, *2*, 164.
[48] J. Zheng, T. Miao, R. Xu, X. Ping, Y. Wu, Z. Lu, Z. Zhang, D. Hu, L. Liu, Q. Zhang, D. Li, Z. Cheng, W. Ma, L. Xie, L. Jiao, *Adv. Mater.* **2021**, *33*, 2101150.
[49] B. Y. Zhang, K. Xu, Q. Yao, A. Jannat, G. Ren, M. R. Field, X. Wen, C. Zhou, A. Zavabeti, J. Z. Ou, *Nat. Mater.* **2021**, *20*, 1073.
[50] A. Zavabeti, P. Aukarasereenont, H. Tuohey, N. Syed, A. Jannat, A. Elbourne, K. A. Messalea, B. Y. Zhang, B. J. Murdoch, J. G. Partridge, M. Wurdack, D. L. Creedon, J. Van Embden, K. Kalantar-Zadeh, S. P. Russo, C. F. McConville, T. Daeneke, *Nat. Electron.* **2021**, *4*, 277.
[51] H. Yu, Q. Liao, Z. Kang, Z. Wang, B. Liu, X. Zhang, J. Du, Y. Ou, M. Hong, J. Xiao, Z. Zhang, Y. Zhang, *SmallSmall* **2020**, *16*, 2005520.
[52] A. Liu, G. Liu, H. Zhu, H. Song, B. Shin, E. Fortunato, R. Martins, F. Shan, *Adv. Funct. Mater.* **2015**, *25*, 7180.
[53] C. W. Shih, A. Chin, C. F. Lu, W. F. Su, *Sci. Rep.* **2018**, *8*, 889.
[54] F. Shan, A. Liu, H. Zhu, W. Kong, J. Liu, B. Shin, E. Fortunato, R. Martins, G. Liu, *J. Mater. Chem. C* **2016**, *4*, 9438.
[55] C. Wang, H. Zhu, Y. Meng, S. Nie, Y. Zhao, B. Shin, E. Fortunato, R. Martins, F. Shan, G. Liu, *IEEE Trans. Electron Devices* **2019**, *66*, 1458.
[56] S. Nie, A. Liu, Y. Meng, B. Shin, G. Liu, F. Shan, *J. Mater. Chem. C* **2018**, *6*, 1393.
[57] B. Liu, M. Köpf, A. N. Abbas, X. Wang, Q. Guo, Y. Jia, F. Xia, R. Weihrich, F. Bachhuber, F. Pielnhofer, H. Wang, R. Dhall, S. B. Cronin, M. Ge, X. Fang, T. Nilges, C. Zhou, *Adv. Mater.* **2015**, *27*, 4423.
[58] L. Li, W. Wang, P. Gong, X. Zhu, B. Deng, X. Shi, G. Gao, H. Li, T. Zhai, *Adv. Mater.* **2018**, *30*, 1706771.
[59] J. Guo, Y. Liu, Y. Ma, E. Zhu, S. Lee, Z. Lu, Z. Zhao, C. Xu, S.-J. Lee, H. Wu, K. Kovnir, Y. Huang, X. Duan, *Adv. Mater.* **2018**, *30*, 1705934.
[60] A. Liu, H. Zhu, S. Bai, Y. Reo, T. Zou, M.-G. Kim, Y.-Y. Noh, *Nat. Electron.* **2022**, *5*, 78.